Exfoliated Molybdenum Disulfide Encapsulated in a Metal Organic Framework for Enhanced Photocatalytic Hydrogen Evolution

Ren Ren, Huilei Zhao, Xiaoyu Sui, Xiaoru Guo, Xingkang Huang, Yale Wang, Qianqian Dong and Junhong Chen *

Department of Mechanical Engineering, University of Wisconsin-Milwaukee, 3200 N Cramer Street, Milwaukee, WI 53211, USA; renren@uwm.edu (R.R.); huilei.g.zhao@gmail.com (H.Z.); xsui@uwm.edu (X.S.); xiaoru@uwm.edu (X.G.); xkhuang@uwm.edu (X.H.); yalewang@uwm.edu (Y.W.); qdong@uwm.edu (Q.D.)
* Correspondence: jhchen@uwm.edu; Tel.: +1-414-229-2615

Abstract: An exfoliated MoS_2 encapsulated into metal-organic frameworks (MOFs) was fabricated as a promising noble-metal-free photocatalyst for hydrogen production under visible light irradiation. The as-synthesized samples were examined by X-ray diffraction (XRD), scanning electron microscopy (SEM), energy dispersive X-ray spectroscopy (EDS), X-ray photoelectron spectroscopy (XPS), and Brunauer–Emmett–Teller (BET) surface analysis. It is well known that bulk MoS_2 is unsuitable for photocatalysis due to its inadequate reduction and oxidation capabilities. However, exfoliated MoS_2 exhibits a direct band gap of 2.8 eV due to quantum confinement, which enables it to possess suitable band positions and retain a good visible-light absorption ability. As a result, it is considered to be an encouraging candidate for photocatalytic applications. Encapsulating exfoliated MoS_2 into MOF demonstrates an improved visible light absorption ability compared to pure MOF, and the highest hydrogen production rate that the encapsulated exfoliated MoS_2 could reach was 68.4 $\mu mol\ h^{-1}g^{-1}$, which was much higher than that of pure MOF. With a suitable band structure and improved light-harvesting ability, exfoliated MoS_2@MOF could be a potential photocatalyst for hydrogen production.

Keywords: exfoliation; MoS_2; MOF; ZIF-8; photocatalyst; hydrogen evolution

1. Introduction

The increase in demand for clean and renewable energy has motivated new studies for developing novel techniques for hydrogen and oxygen production via water splitting [1–5]. Photocatalysis has been shown to be an attractive process for generating H_2 and O_2, using natural sunlight as an irradiation source [6–9]. Lately, transition-metal oxides (TMOs) and transition metal dichalcogenides (TMDs) have been demonstrated to be effective and efficient catalytic materials [10–12]. In order to use visible light, which occupies about 50% of all solar energy, photocatalysts should meet the following requirements in order to effectively convert solar energy into H_2 via photocatalytic water splitting: the conduction band minimum (CBM) must be more negative than the hydrogen evolution potential 0 V vs. normal hydrogen electrode (NHE) (pH = 0) and the valence band maximum (VBM) must be more positive than the water oxidation level +1.23 V vs. NHE (pH = 0), respectively, and all chemical and structural properties must be stable during the photocatalytic reaction [2,4]. The band structure of the semiconductor component and its redox potentials for water splitting are the keys to discovering suitable candidates for photocatalytic hydrogen evolution [4]. For TMOs, WO_3 can act as a steady photocatalyst for O_2 evolution under visible light illumination together with a suitable electron acceptor.

However, the conduction band of the material is located in a more positive position compared to the water reduction potential, and as a consequence, WO_3 cannot reduce H^+ to H_2 directly [13]. For TMDs, CdSe and CdS possess suitable band structures for visible light-driven water splitting, but they are not stable under the photocatalytic reaction conditions due to their photocorrosion properties (poor photoinduced stability) [5,14]. Therefore, the conventional TMOs and TMDs cannot effectively split water under visible light illumination without any modifications.

MOFs have drawn substantial attention in research for their adjustable pore size, large pore volume, high specific surface area, and highly ordered porous structures. Previous studies have mostly focused on MOFs for sensing, drug delivery, batteries and selective catalysis. Their application as photocatalysts, however, has not been thoroughly reported, and their photocatalytic ability is limited as MOFs lack the capacity to absorb visible light [15,16]. While it is well known that bulk MoS_2 is unsuitable for photocatalytic applications owing to its inadequate reduction and oxidation capabilities, exfoliated MoS_2 shows a direct band gap of 1.9~3.9 eV due to quantum confinement. This enables MoS_2 to possess suitable band positions for absorbing visible-light [17–21], and thus MoS_2 is considered to be a great candidate for photocatalytic applications. Therefore, combining MOFs with a visible-light-active photocatalyst, such as encapsulating TMDs into MOFs to produce core-shell structures, offers combined properties that may lead to synergistic functionalities [14,22]. Recently, increasing attention has been centered on applying MOFs, especially the Zeolitic Imidazolate Framework (ZIF-8) structure, to carbon capture, sensing, drug delivery, batteries and selective catalysis, however, their application as photocatalysts to address both environmental issues and the energy crisis has not been thoroughly reported [23–26].

As one of the metal-organic frameworks (MOFs), the zeolitic imidazolate framework-8 (ZIF-8) is constructed by Zn(II) and 2-methylimidazole ligands, and possesses a high specific surface area and outstanding thermal and chemical stability [26]. Although it is extensively applied in adsorption, catalysis, and gas separation [23,26], the photocatalytic properties of ZIF-8 have been inadequately studied. In Zeng et al.'s study, CdS@ZIF-8 with core-shell structures were synthesized by a two-step method. CdS NPs were first stabilized by polyvinylpyrrolidone (PVP) and then ZIF-8 shells were developed on the surface of the CdS cores [14]. The core-shell CdS@ZIF-8 structures were used for photocatalytic H_2 evolution from formic acid and revealed better selectivity for H_2 production compared to the pure CdS nanoparticles, however, the H_2 production rate of the as-prepared samples was limited. This study focused on developing an exfoliated MoS_2@MOF composite to evaluate its potential for photocatalytic hydrogen evolution. The new photocatalyst showed increased absorption in visible light range with an improved hydrogen production rate compared with pure MOF.

2. Results and Discussion

2.1. Morphology

The exfoliated MoS_2@ZIF-8 (denoted as MZ) was synthesized by a two-step method. First, the exfoliated MoS_2 (denoted as EM) was prepared by sonicating the MoS_2/methanol dispersion in an ultrasonic bath. Next, the EM was added in the process of preparing ZIF-8 to obtain MZ. The morphology of the as-prepared MZ was characterized by scanning electron microscopy (SEM) and energy dispersive X-ray spectroscopy (EDS) analyses. Figure 1a,b shows that the MZ comprised of irregular agglomerates, with the particle size ranging from 10 to 30 μm. Figure 1c,d are the EDS elemental mapping results of MZ for the C, N, O, Zn, Mo, and S elements. The Zn, C, and N elements were well dispersed in the MZ particles, while Mo and S elements were clearly encapsulated in the ZIF-8 shell [14]. From the elemental distribution results of the O element, it can be seen that ZnO rarely existed in the MZ without further calcination.
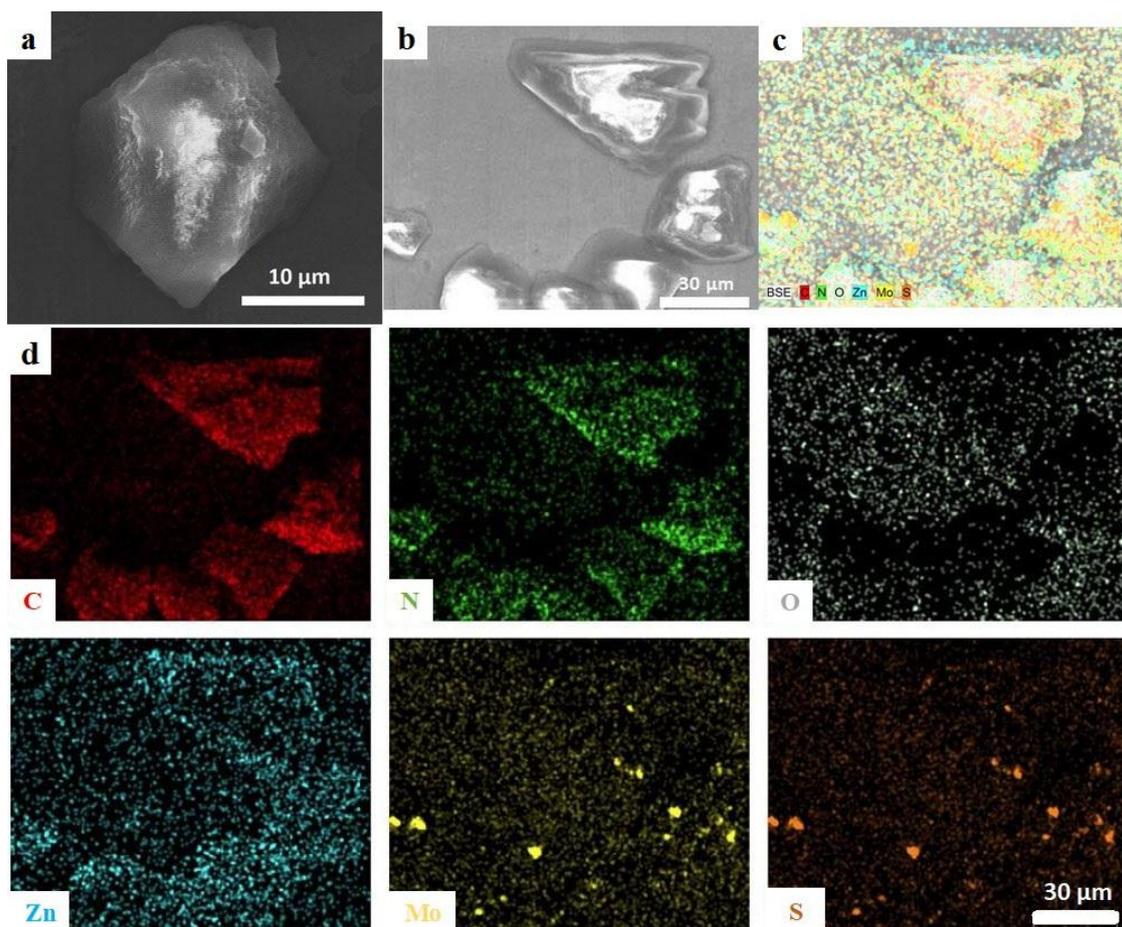
Figure 1. (**a**,**b**) SEM images and (**c**,**d**) energy dispersive X-ray spectroscopy (EDS) elemental mappings of the exfoliated MoS_2@ZIF-8 (MZ) with a copper foil background.

2.2. Structure

XRD analysis was performed in order to investigate and compare the crystal structures of MZ, EM, and ZIF-8. In Figure 2a, all of the peaks of MZ could be assigned to ZIF-8 and MoS_2 in the XRD patterns. The diffraction peaks (2θ) at $14.4°$, $32.7°$, $33.5°$, $35.8°$, $39.5°$, $44.1°$, $49.7°$, and $58.3°$ corresponded to the (002), (100), (101), (102), (103), (006), (105), and (110) crystal planes of 2H-MoS_2 (PDF#37-1742), respectively [27]. The diffraction peaks (2θ) at $10.4°$, $12.7°$, $14.7°$, $16.4°$, and $18.1°$ matched well with the (011), (002), (112), (022), (013), and (222) lattice planes of ZIF-8, respectively [28].

Figure 2b exhibits the N_2 adsorption and desorption isotherms of the MZ and the ZIF-8, respectively. Figure 2c shows the pore size distribution of MZ and ZIF-8. The Brunauer–Emmett–Teller (BET) surface area of ZIF-8 was as high as 1313.8 m^2/g while the BET surface area of MZ reduced to 955.3 m^2/g, but similarities were observed in the surface pore characteristics of the as-synthesized samples. Both curves of the prepared samples could be classified as having Type I isotherm characteristics that suggest their microporous nature. Nonetheless, the existence of large pores suggested that the isotherms changed to Type IV for values of P/P_0 larger than 0.85, which was possibly attributed to intra-aggregate voids [29].

The specific surface areas and average pore diameters of the as-prepared materials were examined based on N_2 adsorption and desorption results (Table 1). XPS analysis was carried out to investigate the chemical states and surface chemical compositions of MZ (Figure 2). The XPS spectra of N1s, O1s, Zn2p, and their simulated decomposition peaks are shown in Figure 2d-f, respectively. For the N1s spectra, the peak appearing at 398.8 eV corresponded to the sp^2-hybridized nitrogen (C=N–C) group [24]. The N1s and C1s peaks could be assigned to the existence of ZIF-8 that was prepared by

2-methylimidazole [22]. The $Zn2p_{1/2}$ and $Zn2p_{3/2}$ peaks (Figure 2f) at the binding energies of 1045.5 and 1022.1 eV were closer to the metallic phase of Zn, which meant that the Zn element mainly stayed in the Zn^0 state. The main peak in the O1s region at 530.3 eV was assigned to carbonates (Figure 2f) [30].
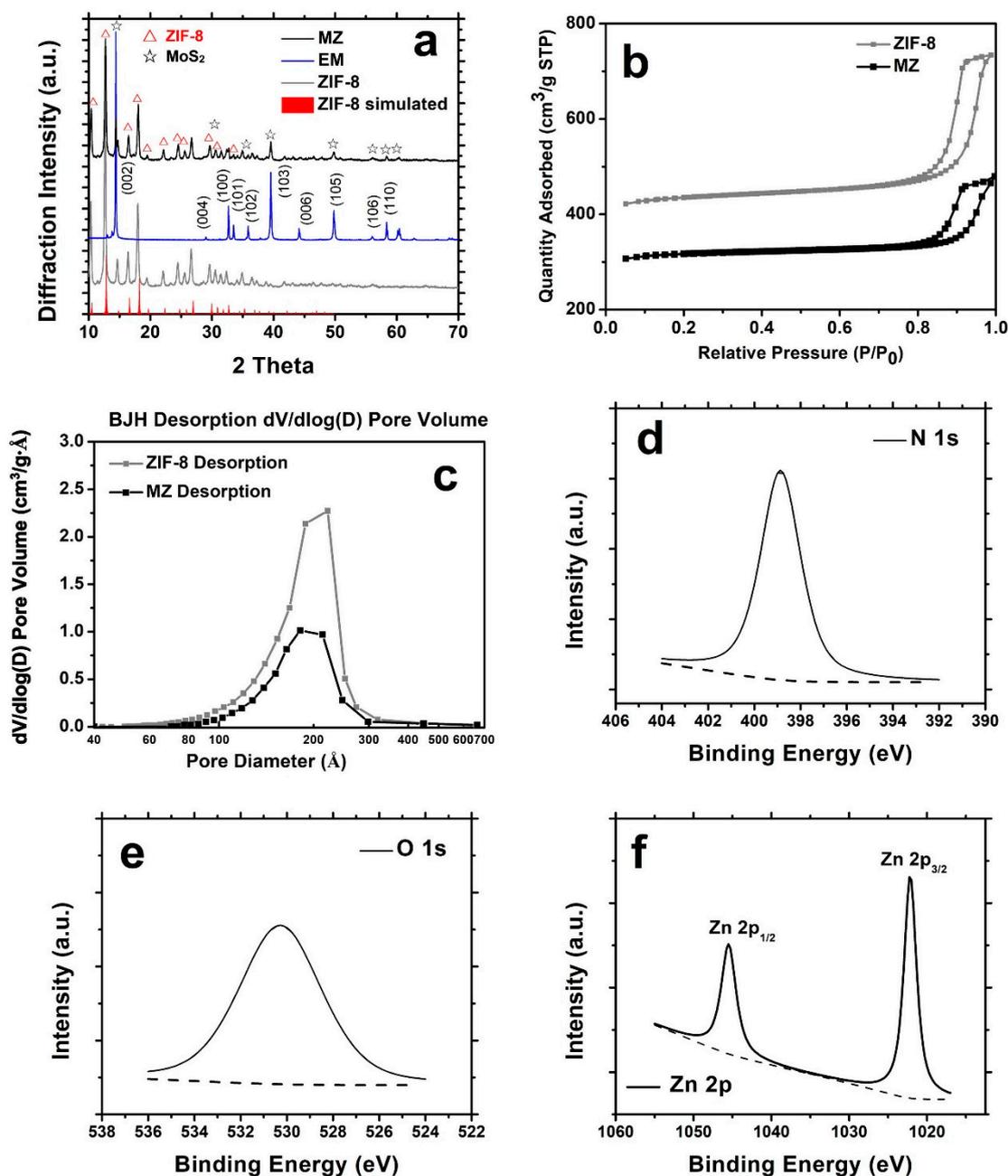
Figure 2. (**a**) Representative XRD patterns of the as-prepared samples; (**b**) N_2 adsorption-desorption isotherms and (**c**) pore size distribution of MZ and zeolitic imidazolate framework (ZIF-8); X-ray photoelectron spectroscopy (XPS) spectrum of (**d**) N1s, € O1s and (**f**) Zn2p of MZ.

Table 1. Surface properties of ZIF-8 and as-synthesized MZ.

Sample	BET Surface Area (m^2/g)	BJH Desorption Average Pore Diameter (Å)	Total Pore Volume (cm^3/g)
ZIF-8	1,313.8	139.0	1.14
MZ	955.3	127.2	0.74

2.3. Optical Properties and Photocatalytic Hydrogen Evolution

Generally, bulk MoS_2 (band gap of 1.2 eV) is unsuitable to act as a photocatalyst, due to its limited reduction and oxidation capability which is required for activating the photocatalytic process. Nonetheless, exfoliated MoS_2 displays a direct band gap of 1.89~3.96 eV stemming from quantum confinement. In Huang et al.'s work, monolayer MoS_2 quantum dots (MQDs) were prepared via a hydrothermal method and exhibited a 3.96 eV of direct band gap compared to monolayer MoS_2 NSs (1.89 eV) [31]. By using scanning tunneling microscopy (STM), another study reported that chemical vapor deposition (CVD)-prepared single-layer MoS_2 possessed a band gap of 2.40 eV [32]. Based on the self-consistent GW_0 ($scGW_0$) calculations, Shi et al. predicted that the quasiparticle (QP) band structures of monolayer MoS_2 exhibited a direct band gap energy of 2.80 eV [33]. This offered the exfoliated MoS_2 the suitable band positions needed to retain the desired visible-light absorption ability. As a result, the exfoliated MoS_2 was considered to be a good candidate for photocatalytic applications.

The optical absorption of ZIF-8, EM, and MZ was examined by UV-Vis absorption spectra (Figure 3). The absorption edge for ZIF-8 (Figure 3a) at ~250 nm without significant absorption in the visible light region suggested a band gap of 5.15 eV. The absorption edge of EM (Figure 3b) was at ~390 nm and showed a limited visible light absorption ability with a band gap of 2.84 eV. However, for EM (a band gap of 3.41 eV), the absorption edge appeared at ~415 nm (Figure 3c), which indicated that EM was effective in the visible light region. The possible mechanism is illustrated in Figure 3d. Methanol (CH_3OH) was used as a sacrificial electron donor to provide protons with electrons in the experiments. CH_3OH was initially oxidized by the excited holes, which generated protons (H^+) with a hydroxyalkyl radical intermediate ($\cdot CH_2OH$). Then $\cdot CH_2OH$ further produced H^+ and electrons that subsequently formed H_2. The photocatalytic performance of MZ was studied by examining the photocatalytic hydrogen production under visible light with a Xe lamp irradiation (AM 1.5 G, 100 mW cm^{-2}). The hydrogen evolution rate for the reported ZIF-8 was 0.01 $\mu mol\ h^{-1}g^{-1}$, and no activity was shown for bulk MoS_2. As shown in Figure 3e, with the coexistence of EM, MZ gave an improved average hydrogen evolution rate of 29.9 $\mu mol\ h^{-1}g^{-1}$.
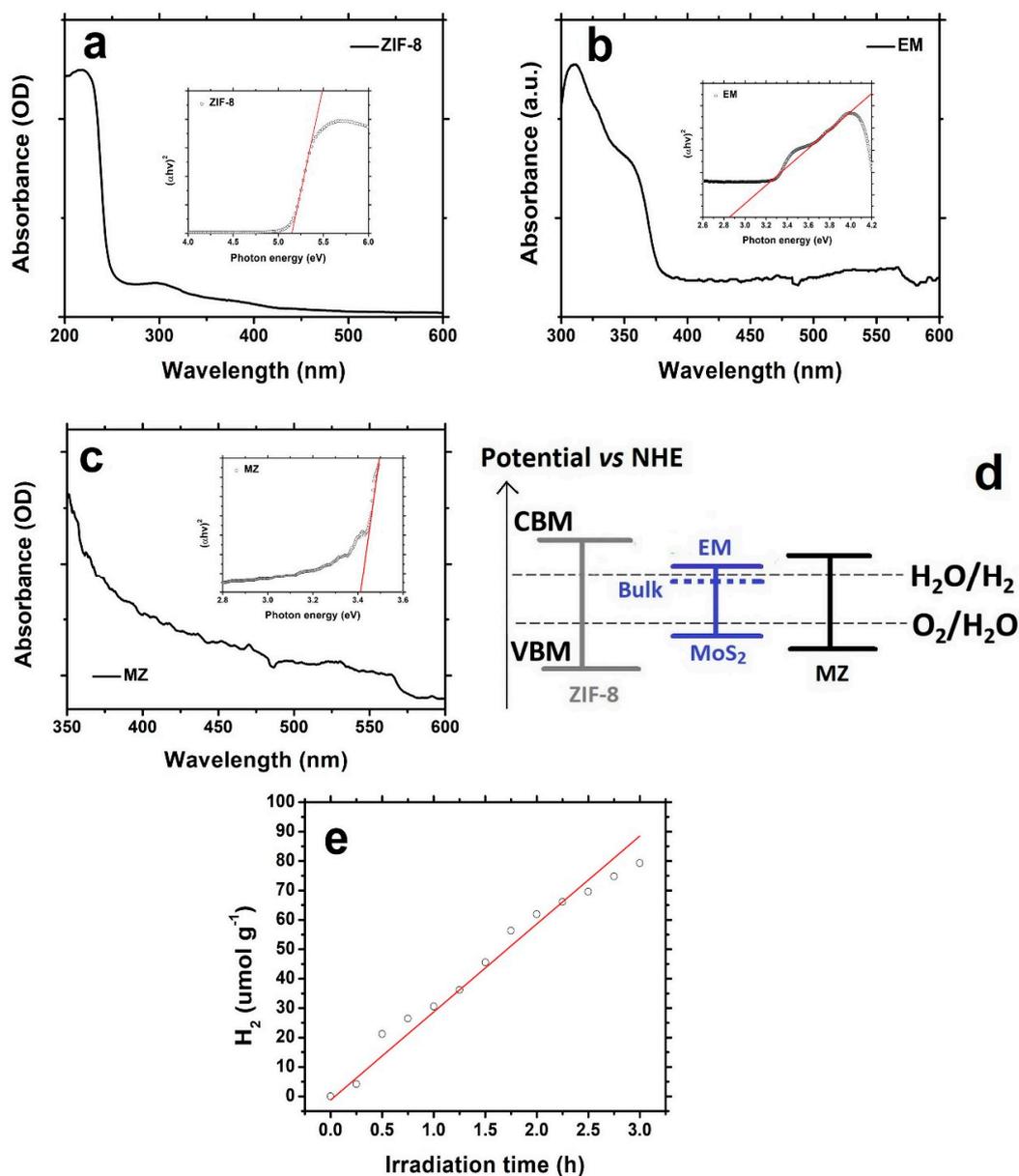
Figure 3. UV-vis absorption spectra and Tauc's plot (inset) for band gap energy determination of (**a**) ZIF-8, (**b**) exfoliated MoS_2 (EM), and (**c**) MZ; (**d**) schematic illustration of the energy band structure of the as-prepared samples; (**e**) photocatalytic hydrogen production rate collected for MZ.

3. Materials and Methods

3.1. Synthesis

The process of synthesizing exfoliated MoS_2 was as follows. 100 mg of MoS_2 bulk powder (purchased from Sigma-Aldrich, St. Louis, MO, USA) was first immersed in 100 mL of methanol (purchased from Sigma-Aldrich, St. Louis, MO, USA). Then exfoliation was achieved by sonicating the dispersion in an ultrasonic bath for 1 h and then probe-sonicating for another 1 h. The bath temperature during sonication was kept below 277 K by immersing the sample in an ice water bath. The top two-thirds of the exfoliated MoS_2 were collected for further experiments.

The process of synthesizing MoS_2@ZIF8 was as follows. Zinc nitrate hexahydrate ($Zn(NO_3)_2 \cdot 6H_2O$), 2.47 mmol) was first added to the exfoliated MoS_2 methanolic solution (25 mL). Next, the resulting solution was added to 25 mL of 2-methylimidazole (19.85 mmol), kept at room temperature and

stirred for 12 h. Lastly, the dispersion was centrifuged three times at 10,000 rpm for 5 minutes and vacuum-dried to obtain MZ.

3.2. Characterization

Structural and elemental characterization of the as-prepared samples were analyzed on a Hitachi (S-4800) scanning electron microscope (Hitachi, Tokyo, Japan). The X-ray powder diffraction investigation was carried out on a Bruker D8 Discover X-ray diffractometer (Bruker, Billerica, MA, USA) equipped with a scintillation counter and a Cu k-alpha radiation (0.15418 nm) reflection mode. Renishaw Raman microscope was used for studying the Raman spectroscopy with an excitation wavelength of 1064. X-ray photoelectron spectroscopy spectra were obtained using a PerkinElemer PHI 5440 ESCA System (PHI-5440, PerkinElemer, Waltham, MA, USA) with monochromatic Al Kα radiation functioning as the X-ray source. The C1s peak located at 285 eV was used as a reference point in this study. ASAP2020 (Micromeritics, Norcross, GA, USA) Brunauer–Emmett–Teller N_2 adsorption-desorption was used to obtain the specific surface area. The N_2 adsorption-desorption tests were conducted at 77 K using a Quantachrome Autosorb gas-sorption system (Quantachrome, Boynton Beach, FL, USA). All the samples were degassed at 200 °C for 2 h before the examinations. The BET method was used to estimate the sample-specific surface area.

3.3. Measurements

Compressed N_2 was the carrier gas used for examining the performance of hydrogen evolution. The N_2 carrier gas was regulated by two mass flow controllers continuously moving through a bubbler which contained 5 vol.% methanol mixed in de-ionized water to create a water-methanol vapor system. Methanol in the mixture acted as a sacrificial electron donor to provide H^+ with electrons. The volume fraction of water (2.2%) and methanol (0.6%) in the mixed gas at 20 °C was evaluated through the saturation vapor pressure–temperature profile, which was balanced with the N_2 carrier gas. The mixed gas was then transferred into a photoreactor. Next, 25 mg samples were prepared on a glass fiber filter and placed in the middle of the tube reactor. A solar light simulator (Newport Oriel, Sol1ATM 94021A, Newport, Irvine, CA, USA) equipped with a Xe lamp and an Air Mass 1.5 global filter (AM 1.5 G, 100 mW cm^{-2}) with a normal incidence compared to the sample served as the photo-excitation source. Before the illumination, the reactor was initially cleaned by the N_2 at a flow rate of 200 ml/min for 1 h and next at 2 mL/min for 1 h. The flow rate of carrier gas was maintained at 2 mL/min during the illumination and the sample was recorded every 15 min by an automated valve to control the gas chromatography (GC, Agilent 7890A, Agilent, Santa Clara, CA, USA). The GC in this study used a thermal conductivity detector (TCD).

4. Conclusions

In summary, a facile and effective method to synthesize exfoliated MoS_2@ZIF-8 hybrids with improved photocatalytic activity in hydrogen production was demonstrated. Encapsulating exfoliated MoS_2 into ZIF-8 could maintain the desired porous structural characteristics of MOFs and the large specific surface area (955.3 m^2/g for MZ) that are both critical for photocatalysis. The obtained hybrid photocatalyst exhibited an enhanced absorption (~415 nm) in visible light range compared to pure ZIF-8 (~250 nm). As a result, the as-prepared MoS_2@ZIF-8 hybrids possessed a more desirable band gap structure (3.41 eV) than ZIF-8 (5.15 eV), which lead to an enhanced efficiency for photocatalysis. In comparison with the pristine ZIF-8, the MZ exhibited substantially enhanced photocatalytic activity for hydrogen production at 29.9 $\mu mol\ h^{-1}g^{-1}$ under visible-light irradiation. The improved photocatalytic performance could be ascribed to the larger specific surface area, suitable band structure, and improved visible light-harvesting ability resulting from the hybrid structure.

Conflicts of Interest: The authors declare no conflicts of interest.

References

1. Chaubey, R.; Sahu, S.; James, O.O.; Maity, S. A review on development of industrial processes and emerging techniques for production of hydrogen from renewable and sustainable sources. *Renew. Sustain. Energy Rev.* **2013**, *23*, 443–462. [CrossRef]

2. Hisatomi, T.; Kubota, J.; Domen, K. Recent advances in semiconductors for photocatalytic and photoelectrochemical water splitting. *Chem. Soc. Rev.* **2014**, *43*, 7520–7535. [CrossRef]

3. Khan, S.U.; Al-Shahry, M.; Ingler, W.B., Jr. Efficient photochemical water splitting by a chemically modified n-TiO_2. *Science* **2002**, *297*, 2243–2245. [CrossRef]

4. Kudo, A.; Miseki, Y. Heterogeneous photocatalyst materials for water splitting. *Chem. Soc. Rev.* **2009**, *38*, 253–278. [CrossRef] [PubMed]

5. Zhong, Y.Y.; Shao, Y.L.; Ma, F.K.; Wu, Y.Z.; Huang, B.B.; Hao, X.P. Band-gap-matched CdSe QD/WS_2 nanosheet composite: Size-controlled photocatalyst for high-efficiency water splitting. *Nano Energy* **2017**, *31*, 84–89. [CrossRef]

6. Clarizia, L.; Russo, D.; Di Somma, I.; Andreozzi, R.; Marotta, R. Hydrogen Generation through Solar Photocatalytic Processes: A Review of the Configuration and the Properties of Effective Metal-Based Semiconductor Nanomaterials. *Energies* **2017**, *10*, 1624. [CrossRef]

7. Hsieh, S.H.; Lee, G.J.; Chen, C.Y.; Chen, J.H.; Ma, S.H.; Horng, T.L.; Chen, K.H.; Wu, J.J. Synthesis of Pt Doped Bi_2O_3/RuO_2 Photocatalysts for Hydrogen Production from Water Splitting Using Visible Light. *J. Nanosci. Nanotechnol* **2012**, *12*, 5930–5936. [CrossRef] [PubMed]

8. Zhang, Q.Y.; Li, Y.; Ackerman, E.A.; Gajdardziska-Josifovska, M.; Li, H.L. Visible light responsive iodine-doped TiO_2 for photocatalytic reduction of CO_2 to fuels. *Appl. Catal. A Gen.* **2011**, *400*, 195–202. [CrossRef]

9. Zou, Z.; Ye, J.; Sayama, K.; Arakawa, H. Direct splitting of water under visible light irradiation with an oxide semiconductor photocatalyst. *Nature* **2001**, *414*, 625–627. [CrossRef]

10. Choi, W.; Choudhary, N.; Han, G.H.; Park, J.; Akinwande, D.; Lee, Y.H. Recent development of two-dimensional transition metal dichalcogenides and their applications. *Mater. Today* **2017**, *20*, 116–130. [CrossRef]

11. Duan, X.D.; Wang, C.; Pan, A.L.; Yu, R.Q.; Duan, X.F. Two-dimensional transition metal dichalcogenides as atomically thin semiconductors: Opportunities and challenges. *Chem. Soc. Rev.* **2015**, *44*, 8859–8876. [CrossRef] [PubMed]

12. Johari, P.; Shenoy, V.B. Tuning the Electronic Properties of Semiconducting Transition Metal Dichalcogenides by Applying Mechanical Strains. *ACS Nano* **2012**, *6*, 5449–5456. [CrossRef]

13. Suzuki, T.; Watanabe, H.; Oaki, Y.; Imai, H. Tuning of photocatalytic reduction by conduction band engineering of semiconductor quantum dots with experimental evaluation of the band edge potential. *Chem. Commun.* **2016**, *52*, 6185–6188. [CrossRef] [PubMed]

14. Zeng, M.; Chai, Z.G.; Deng, X.; Li, Q.; Feng, S.Q.; Wang, J.; Xu, D.S. Core-shell CdS@ZIF-8 structures for improved selectivity in photocatalytic H_2 generation from formic acid. *Nano Res.* **2016**, *9*, 2729–2734. [CrossRef]

15. Jing, Y.Q.; Wang, J.N.; Yu, B.H.; Lun, J.; Cheng, Y.Y.; Xiong, B.; Lei, Q.; Yang, Y.F.; Chen, L.Y.; Zhao, M.Q. A MOF-derived ZIF-8@$Zn_{1-x}Ni_xO$ photocatalyst with enhanced photocatalytic activity. *RSC Adv.* **2017**, *7*, 42030–42035. [CrossRef]

16. Zhou, F.; Zhou, J.J.; Gao, X.C.; Kong, C.L.; Chen, L. Facile synthesis of MOFs with uncoordinated carboxyl groups for selective CO_2 capture via postsynthetic covalent modification. *RSC Adv.* **2017**, *7*, 3713–3719. [CrossRef]

17. Ambrosi, A.; Sofer, Z.; Pumera, M. 2H -> 1T phase transition and hydrogen evolution activity of MoS$_2$, MoSe$_2$, WS$_2$ and WSe$_2$ strongly depends on the MX$_2$ composition. *Chem. Commun.* **2015**, *51*, 8450–8453. [CrossRef] [PubMed]

18. Bai, S.; Wang, L.M.; Chen, X.Y.; Du, J.T.; Xiong, Y.J. Chemically exfoliated metallic MoS$_2$ nanosheets: A promising supporting co-catalyst for enhancing the photocatalytic performance of TiO$_2$ nanocrystals. *Nano Res* **2015**, *8*, 175–183. [CrossRef]

19. Gopalakrishnan, D.; Damien, D.; Shaijumon, M.M. MoS$_2$ Quantum Dot-Interspersed Exfoliated MoS$_2$ Nanosheets. *Acs Nano* **2014**, *8*, 5297–5303. [CrossRef] [PubMed]

20. Li, F.; Li, J.; Cao, Z.; Lin, X.Q.; Li, X.Z.; Fang, Y.Y.; An, X.C.; Fu, Y.; Jin, J.; Li, R. MoS$_2$ quantum dot decorated RGO: A designed electrocatalyst with high active site density for the hydrogen evolution reaction. *J. Mater. Chem. A* **2015**, *3*, 21772–21778. [CrossRef]

21. Shen, M.; Yan, Z.P.; Yang, L.; Du, P.W.; Zhang, J.Y.; Xiang, B. MoS$_2$ nanosheet/TiO$_2$ nanowire hybrid nanostructures for enhanced visible-light photocatalytic activities. *Chem. Commun.* **2014**, *50*, 15447–15449. [CrossRef]

22. Kong, R.M.; Zhao, Y.; Zheng, Y.Q.; Qu, F.L. Facile synthesis of ZnO/CdS@ZIF-8 core-shell nanocomposites and their applications in photocatalytic degradation of organic dyes. *RSC Adv.* **2017**, *7*, 31365–31371. [CrossRef]

23. Gong, X.; Wang, Y.J.; Kuang, T.R. ZIF-8-Based Membranes for Carbon Dioxide Capture and Separation. *ACS Sustain. Chem. Eng.* **2017**, *5*, 11204–11214. [CrossRef]

24. He, F.; Chen, G.; Zhou, Y.S.; Yu, Y.G.; Li, L.Q.; Hao, S.; Liu, B. ZIF-8 derived carbon (C-ZIF) as a bifunctional electron acceptor and HER cocatalyst for g-C$_3$N$_4$: Construction of a metal-free, all carbon-based photocatalytic system for efficient hydrogen evolution. *J. Mater. Chem. A* **2016**, *4*, 3822–3827. [CrossRef]

25. He, L.; Li, L.; Zhang, L.Y.; Xing, S.X.; Wang, T.T.; Li, G.Z.; Wu, X.T.; Su, Z.M.; Wang, C.G. ZIF-8 templated fabrication of rhombic dodecahedron-shaped ZnO@SiO$_2$, ZIF-8@SiO$_2$ yolk-shell and SiO$_2$ hollow nanoparticles. *Crystengcomm* **2014**, *16*, 6534–6537. [CrossRef]

26. Wu, M.; Ye, H.L.; Zhao, F.Q.; Zeng, B.Z. High-Quality Metal-Organic Framework ZIF-8 Membrane Supported on Electrodeposited ZnO/2-methylimidazole Nanocomposite: Efficient Adsorbent for the Enrichment of Acidic Drugs. *Sci. Rep.* **2017**, *7*. [CrossRef] [PubMed]

27. Gao, D.Q.; Si, M.S.; Li, J.Y.; Zhang, J.; Zhang, Z.P.; Yang, Z.L.; Xue, D.S. Ferromagnetism in freestanding MoS$_2$ nanosheets. *Nanoscale Res. Lett.* **2013**, *8*. [CrossRef] [PubMed]

28. Yang, X.B.; Qiu, L.Q.; Luo, X.T. ZIF-8 derived Ag-doped ZnO photocatalyst with enhanced photocatalytic activity. *RSC Adv.* **2018**, *8*, 4890–4894. [CrossRef]

29. Da Silva, J.D.F.; Malo, D.L.; Bataglion, G.A.; Eberlin, M.N.; Ronconi, C.M.; Alves, S.; de Sa, G.F. Adsorption in a Fixed-Bed Column and Stability of the Antibiotic Oxytetracycline Supported on Zn(II)-[2-Methylimidazolate] Frameworks in Aqueous Media. *PLoS ONE* **2015**, *10*. [CrossRef]

30. He, L.; Li, L.; Wang, T.T.; Gao, H.; Li, G.Z.; Wu, X.T.; Su, Z.M.; Wang, C.G. Fabrication of Au/ZnO nanoparticles derived from ZIF-8 with visible light photocatalytic hydrogen production and degradation dye activities. *Dalton Trans.* **2014**, *43*, 16981–16985. [CrossRef] [PubMed]

31. Huang, H.; Du, C.C.; Shi, H.Y.; Feng, X.; Li, J.; Tan, Y.L.; Song, W.B. Water-Soluble Monolayer Molybdenum Disulfide Quantum Dots with Upconversion Fluorescence. *Part. Part. Syst. Charact.* **2015**, *32*, 72–79. [CrossRef]

32. Huang, Y.L.; Chen, Y.F.; Zhang, W.J.; Quek, S.Y.; Chen, C.H.; Li, L.J.; Hsu, W.T.; Chang, W.H.; Zheng, Y.J.; Chen, W.; et al. Bandgap tunability at single-layer molybdenum disulphide grain boundaries. *Nat. Commun.* **2015**, *6*, 6298. [CrossRef] [PubMed]

33. Shi, H.L.; Pan, H.; Zhang, Y.W.; Yakobson, B.I. Quasiparticle band structures and optical properties of strained monolayer MoS$_2$ and WS$_2$. *Phys. Rev. B* **2013**, *87*, 155304. [CrossRef]